Chemical Synthesis

Research Article

CoFe$_2$O$_4$ nanoparticles as a bifunctional agent on activated porous carbon for battery-type asymmetrical supercapacitor

Qiang Qu[1,2], Zhuo Chen[1,2], Guo-Tao Sun[1,2], Ling Qiu[1,2], Ming-Qiang Zhu[1,2,*] iD

[1]College of Mechanical and Electronic Engineering, Northwest A&F University, Yangling 712100, Shaanxi, China.
[2]Northwest Research Center of Rural Renewable Energy Exploitation and Utilization of M.O.A, Northwest A&F University, Yangling 712100, Shaanxi, China.

*****Correspondence to:** Prof. Ming-Qiang Zhu, College of Mechanical and Electronic Engineering, Northwest A&F University, No. 3 Taicheng Road, Yangling 712100, Shaanxi, China. E-mail: zmqsx@nwsuaf.edu.cn

Abstract

The low performance of electrode materials is the main obstacle limiting the development of the supercapacitor industry, which can be solved by doping cobalt ferrate nanoparticles (NPs) with carbon materials. Herein, the composites of CoFe$_2$O$_4$ based on activated carbon (AC) were successfully prepared using a one-step solvothermal method and subsequently applied in anodes of battery-type asymmetrical supercapacitors. The effect of solvothermal temperature and heating time on the composite characteristic was systematically evaluated. The electrochemical analysis in the three-electrode system revealed that modified activated carbon heated at 140 °C for 24 h (140MAC24) displayed excellent specific capacitance of 571.36 F/g at the current density of 0.2 A/g due to the synergistic effect of the double-layer and faradic capacitance. Moreover, iron and cobalt elements in CoFe$_2$O$_4$ could change into the oxide form to accelerate charge in potential range window of -1.0 to -0.2 V and discharge from -0.2 to 0.2 V, respectively. Meanwhile, the result of assessing economic feasibility suggested the splendid availability of 140MAC24 electrodes. Additionally, the assembled supercapacitor displayed the outstanding specific capacitance of 171.31 F/g in the potential window of 1.8 V, energy density of 43.5 Wh/kg at the current density of 0.2 A/g, and capacitance retention rate of 82.49% after 10,000 cycles. The excellent electrochemical properties demonstrated that CoFe$_2$O$_4$ could be used as a bifunctional agent for enhancing supercapacitive performance.

Keywords: CoFe$_2$O$_4$ nanoparticle, activated carbon, bifunctional agent, battery-type asymmetrical supercapacitor, *Eucommia ulmoides Oliver*-wood

INTRODUCTION

At present, the rapid consumption of finite fossil resources and the gradually worsening environment have caused gasoline engine vehicles to be replaced by electric vehicles[1]. Subsequently, the urgent demand for effective electricity storage is one of the most important concerns to be solved[2]. The effective solution could be widely using reproducible energy such as tidal energy, solar power, or biomass energy[3], and producing the high-performance energy storage devices, such as supercapacitors[4], Li-ion[5], sodium-ion[6,7], lithium-selenium[8], aqueous ammonium-ion[9], aqueous Zn-ion[10], and Zn-air batteries[11,12], and conventional capacitors[13]. Among these, the supercapacitors, with the superiorities of rapid charging-discharging occasions, high lifespan and power density, could meet the practical requirements and exhibit great potential in the field of energy storage[14-16]. However, their industrialization has not developed on a large scale, which is mainly limited by the structural properties and electrochemical capacity of electrode materials.

In general, carbon materials such as carbon nanotubes, graphene, and activated carbon (AC) are extensively studied to store energy by transmitting ions in the pore structure, implying the great superiority in the application of supercapacitor electrodes[17]. As a three-dimensional material, AC displays better electrochemical performance and feasibility for further enhancement. Besides, it could be produced from renewable biomass feedstock using the physical or chemical activation method, which exhibited the porous structure and complex channels[13,18]. Hence, the strategy of converting biomass sources to AC material applied in the supercapacitor electrode is feasible to solve the energy storage crisis and accomplish the economic value[19,20]. The energy storage property of AC is being investigated, and it has become indispensable for energy carbon material. The large micropore dominant carbon (1-2 nm) produced with the flaxseed residues as feedstock displayed the outstanding electrochemical properties of 398 F/g at a current density of 0.5 A/g[21]. At higher current densities, the supercapacitor exhibited poor electrochemical performance. Therefore, AC-based electrodes still exhibit the poor electrochemical performance under the condition of a high charge-discharge rate due to the physical adsorption mechanism of charge and discharge.

In order to improve the high-rate capability, researchers have attempted to synthesize a composite composed of metal oxide and carbon material, which could possess both imaginary and real capacitance for supercapacitors[22]. Several transition metal oxides such as V_2O_5[23], Fe_2O_3[24], Co_3O_4[25], WO_3[26], and $CoFe_2O_4$[27] have been widely employed for supercapacitors in order to enhance the pseudocapacitance. In particular, $CoFe_2O_4$ possesses the Co (II) and Fe (III) elements severally distributed in the tetrahedral and the octahedral sites, which exhibits a large theoretical capacitance of 916 mAh/g[15]. Furthermore, binary metal oxides may be able to compensate for the narrow range of working voltage in the single metal atom and may generate bifunctional effects to promote the electrochemical properties. This advantage could provide a longer reaction period, contributing to the ion transfer and electron generation in the supercapacitor system. Our team has synthesized the spinel-type $CoFe_2O_4$ and subsequently anchored it on AC using the solvothermal synthetization methods[15]. The composite displayed a well-built porous structure [specific surface area (SSA) = 1,226.5 m^2/g] and a high capacitance (596.26 F/g) at the scanning rate of 0.005 V/s in a three-electrode system. Besides, it was also found that the synthetization conditions are important to the formation, size of $CoFe_2O_4$ nanoparticles (NPs), and pore form of the composite[28]. In this case, as the two most critical factors for the solvothermal method, the effects of the solvothermal temperature and heating time on the characteristics of $CoFe_2O_4$ composites based on the carbon material are rarely researched. The $CoFe_2O_4$ particles could provide metal ions and electrons by redox reactions with the electrolyte, which may be restricted by the different work voltage conditions. Therefore, it is significant to explore the function mechanism of $CoFe_2O_4$ on the electrochemical properties of AC electrodes.

Herein, a composite of AC and $CoFe_2O_4$ NPs was synthesized through a hydrothermal method. Furthermore, the influence of hydrothermal temperature and duration time was systemically investigated. The results demonstrated that modified activated carbon heated at 140 °C for 24 h (140MAC24) displayed excellent specific capacitance of 571.36 F/g due to the synergistic effect of the double-layer and faradic capacitance. Moreover, iron and cobalt oxide in $CoFe_2O_4$ could change into the oxide form to accelerate charge in potential range window of -1.0 to -0.2 V and discharge from -0.2 to 0.2 V, respectively. Additionally, the assembled supercapacitor displayed an outstanding specific capacitance of 171.31 F/g in the potential window of 1.8 V, an energy density of 43.5 Wh/kg, and a capacitance retention rate of 82.49% after 10,000 cycles.

EXPERIMENTAL
Material and agents
Eucommia ulmoides Oliver (EUO)-wood was harvested and collected from the experimental plot in the Northwest Agriculture and Forestry University, Yangling District, Shaanxi Province, China[15]. After removing the bark and leaf, the EUO-wood was dried and smashed to obtain a wood meal (40-60 meshes). All chemicals (NaOH, HCl, $FeCl_3 \cdot 6H_2O$, $CoCl_2 \cdot 6H_2O$, and $FeSO_4 \cdot 7H_2O$) in analytical pure (≥ 99.0%) were acquired from Aladdin Biochemical Pharmaceutical Co., Ltd (Shanghai, China).

Preparation of AC derived from EUO-wood
AC derived from the EUO-wood was synthesized via one-step activation using the same technology in previous work[15]. The EUO-wood (10.00 g) was impregnated by 25 wt% phosphoric acid for 9 h with the solid to liquid ratio of 1:4. Then, the 12 h-drying desiccative sample was transferred to a tubular furnace to prepare AC under certain conditions of pyrolysis temperature (400 °C), heating rate (5 °C/min), holding period (6 h), and N_2 flow rate (600 mL/min). After that, the AC sample was rinsed with deionized water to be neutral for further utilization.

Preparation of modified AC by solvothermal method
The preparation of modified activated carbons (MACs) was conducted by a solvothermal method under different conditions of the heating temperature (120, 140, and 160 °C) and the holding time (18, 24, and 30 h) [Figure 1A]. The modification solution was prepared by dissolving $FeCl_3 \cdot 6H_2O$ (3.917 g), $FeSO_4 \cdot 7H_2O$ (2.000 g) and $CoCl_2 \cdot 6H_2O$ (5.235 g) in deoxidized and deionized water (100 mL). The AC precursor (5.000 g) was mixed with the modification solution using the magnetic stirrer at 90 °C for 1 h, and then NaOH powder (4.0640 g) was blended in the above suspension for 2 h. The obtained precipitate was transferred in the stainless reaction kettle lined with a tetrafluoroethylene tank (100 mL volume), which was subsequently heated in the muffle furnace at the determined temperature for 24 h. Finally, the solid products were washed with deionized water and ethyl alcohol to be neutral, and the samples were named 120MAC24, 140MAC24 and 160MAC24, respectively. Additionally, a part of the above precipitate was also heated in the same heating way at 140 °C for 18 and 30 h, which were labeled as 140MAC18 and 140MAC30, respectively.

Characterization of AC and MACs
The porous structures of AC and MACs were characterized by scanning electron microscopy and energy dispersive X-ray Detector (SEM-EDX) (TM3000, Hitachi, Japan)[29] and transmission electron microscope (TEM) (Talos F200X S/TEM)[15]. The Brunauer-Emmett-Teller (BET) surface area, Barrett-Joyner-Halenda (BJH) pore size distribution, and pore volume were measured following the multipoint N_2 adsorption method using Tristar II 3020 (Micromeritics, Shanghai, China)[30]. The phase structure and the surface elemental compositions were identified by an X-ray diffractometer (XRD) with a Cu Kα radiation (λ = 1.5418) in 2θ range from 10° to 80° (D8 ADVANCE A25, Bruker, German) and X-ray photoelectron
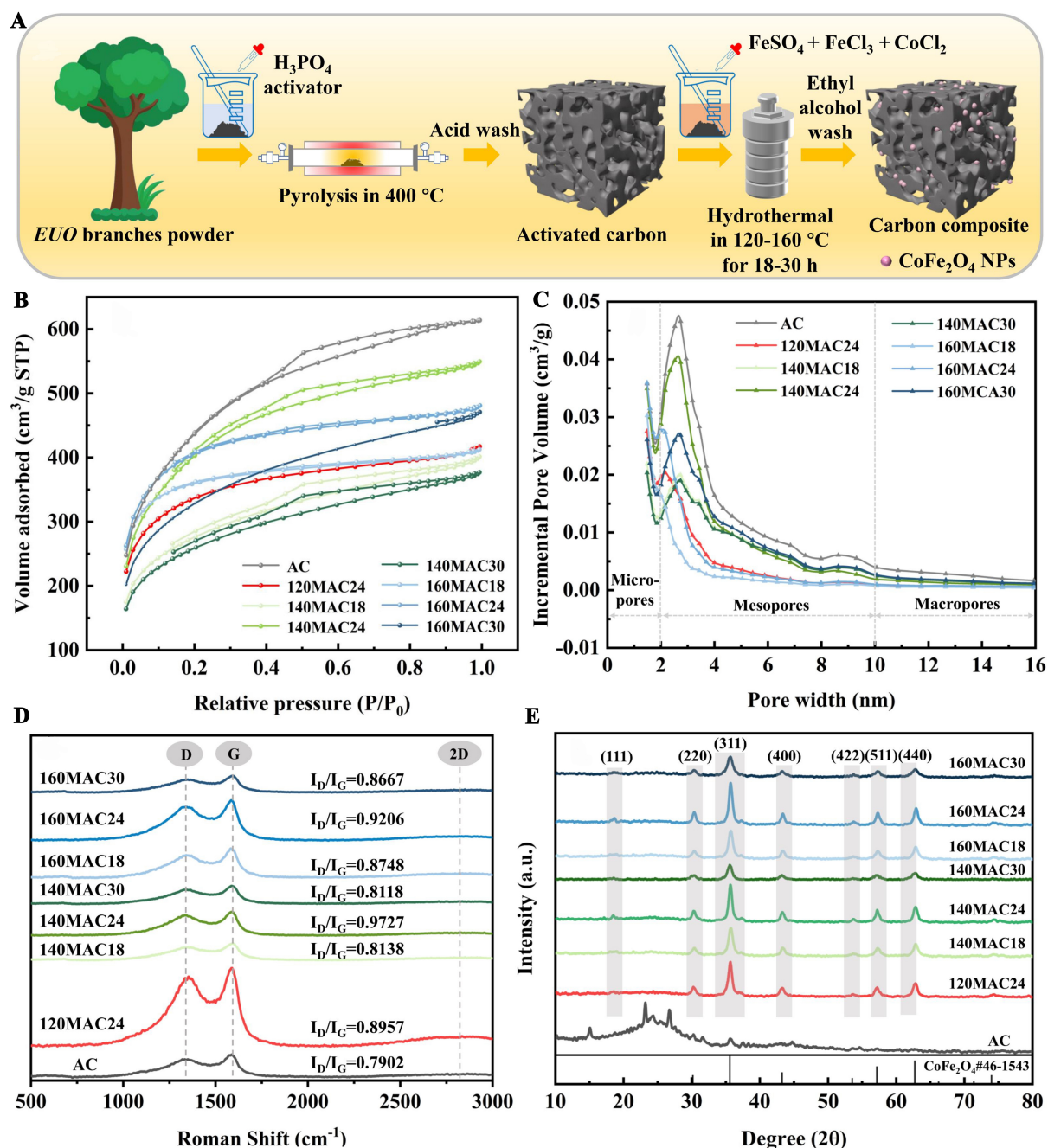
Figure 1. (A) The schematic illustration of magnetic carbon synthesized via the hydrothermal method; (B) N$_2$ adsorption-desorption isotherms; (C) pore diameter distribution; (D) XRD; and (E) Roman spectrum of AC and MACs. XRD: X-ray diffractometer; AC: activated carbon; MACs: modified activated carbons.

spectroscopy (XPS) (Thermo Fisher K-Alpha, England), respectively[18]. XPS spectra were analyzed using Avantage Thermo software (Version 2.9.9.9). The Fourier transform infrared spectroscopy (FTIR) (Vertex70, Bruker, German) with a wavenumber range from 4,000 to 400 cm^{-1} at a resolution of 4 cm^{-1} was analyzed to characterize the functional groups. The Raman spectra of samples were recorded at ambient temperature on a Raman microscope (Horiba JobinYvon, Longjumeau, France) equipped with a confocal microscope (Olympus BX51, Tokyo, Japan) and a motorized x and y stage with an argon-ion laser at an

excitation wavelength of 532 nm[31].

Measurements of electrochemical and supercapacitive performance
AC or MACs were the active material in the electrode, which contained 80 wt% of AC or MACs, 10 wt% carbon black (SUPER-P, TIMCAL) and 10 wt% of polytetrafluoroethylene (PTFE, ALDRICH). The electrochemical performance measurement was conducted in the three-electrode system. The mixed films covered on stainless steel mesh were used as working electrodes in which the active material weight reached 3.2 mg. The platinum foil was employed as the counter electrode, the Hg/HgO electrode was taken as the reference electrode, and 6 M KOH was the electrolyte. Then, the supercapacitive properties were evaluated in the 2032 button cell system. In detail, the mixed films with the active material weight of 2 mg/cm² were covered in copper foil. The AC film was taken as the cathode, and the MAC film was used as the anode. Meanwhile, 6 M KOH was the electrolyte, and glass fiber was the separator.

All the cyclic voltammetry (CV) experiments were conducted on an electrochemical working station (CHI660E, Shanghai, China). The potential window ranged from -1.0 to +0.2 V in the alkaline electrolyte (6 M KOH). The electrical impedance spectroscopy (EIS) technique was performed on an electrochemical workstation (Zahner Im6ex), and the frequency ranged from 100 kHz to 10 mHz with an alternating current (ac) signal amplitude of 5 mV at open circuit potential. Galvanostatic charge-discharge (GCD) experiments were conducted using a Land Battery test System (Land, China) and the charging-discharging current densities ranged from 0.2 to 5 A/g. The specific capacitance (C_s, F/g), energy density (E, Wh/kg), and power density (P, W/kg) were calculated by

$$C_s = I \times \Delta t / (m \times \Delta v) \tag{1}$$

$$C_s = Q / (m \times \Delta v) \tag{2}$$

$$E = 0.5 \, C_s \Delta V^2 / 3.6 \tag{3}$$

$$P = 3600 \, E / \Delta t \tag{4}$$

where I was the current (A), m was the weight of activated material (g), Δt was the charge and discharge time, Q was the fitting area of CV curves, and ΔV was the voltage window. The CV curve of the electrodes was obtained at different scanning rates (5, 10, 20, 50 mV/s), and the potential window ranges from -1.0 to 0 V. The EIS data were collected at a frequency between 100 kHz and 10 mHz with an ac signal amplitude of 5 mV.

The economic assessment of synthesizing AC and MAC
The economic assessment of the carbon products by different preparation processes was conducted based on unit of specific capacitance divided by cost of synthesis and an operation period[32]. The cost involved expenditures for the electricity and material consumption but did not include the cost of equipment, building, labor, and overhead production[29]. In detail, the parameters of synthesizing different products were listed in Supplementary Tables 1 and 2.

RESULTS AND DISCUSSION
The structure and morphological characterization of AC and MACs
N_2 adsorption-desorption isotherms of the AC and MACs increased sharply at low and high relative pressures, indicating the major microporous and macroporous structures in these materials, respectively

[Figure 1B][33]. The hysteresis loop occurring under medium relative pressure conditions appeared on the curves due to the existence of mesopores[34]. Among all solvothermal products, the isotherm of 140MAC24 appeared to have the most distinct shape, implying the greatest mesopore distribution, which was confirmed by Figure 1C. The porous properties of all samples showed that the SSA of AC (1,503.70 m²/g) was higher than that of MACs, which may be attributed to the blockage caused by metal particles [Table 1]. Among MACs, 140MAC24 has the highest SSA of 1,377.69 m²/g, which was superior to that of 120MAC24 (1,133.07 m²/g) and 160MAC24 (1,355.56 m²/g). This phenomenon implied that proper enhancement of the solvothermal reaction temperature is conducive to the development of the micropore structure and excessively high reaction temperature could cause environmental pressure, resulting in pore collapse and damage to porosity. Meanwhile, by comparing the group of MACs synthesized under the same solvothermal temperature with different heating times, the SSA values of 140MAC18 and 160MAC18 were higher than those of 140MAC30 and 160MAC30 but lower than those of 140MAC24 and 160MAC18. The results demonstrated that increasing heating time could exert a helpful influence on pore development. However, prolonging reaction time could provide more energy for creating channel shells, resulting in the micropore fracture and the macropore formation. This could explain the better priority of 160MAC24 than 120MAC24 as the larger heating and cooling heating time was conducive to developing the pore structure[35]. Among all MAC samples, the outstanding porosity of 140MAC24 could undoubtedly promote the diffusion and transference of the electrolyte ions to the interior of the electrode. Meanwhile, the weak transfer resistance could facilitate the charge storage[36].

The graphitization extent of the AC and MACs was evaluated using Raman spectroscopy [Figure 1D]. The presence of two distinct peaks at 1,342 and 1,581 cm⁻¹ may be attributed to the D- and G-band, respectively. These bands were indicative of the disordered carbon and ordered graphite crystalline structures, as supported by previous research[37]. The presence of a wide peak seen at around 2,750 cm⁻¹ was ascribed to the 2D-band, which signified the existence of layered carbon structures[38]. The value of I_D/I_G, calculated as the ratio of the intensities of both bands, could indicate the extent of graphitization and the conductivity of the material[31]. The I_D/I_G value of MAC was significantly higher than that of AC due to the existence of Co and Fe compound NPs. Among all MAC samples, 140MAC24 exhibited the highest graphitization degree ($I_D/I_G = 0.9727$), which could be consistent with the superiority of the priority mentioned above. Moreover, this phenomenon implied the great defects of the porous structure and the disordered structure in 140MAC24, which was conducive to providing more contact area for the electrolyte ion transport, increasing the material wettability, and further enhancing the charge storage[37]. In addition, the I_D/I_G values of MACs prepared under different conditions presented the similar tends to the above BET results.

The XRD spectra of AC and MACs were characterized by the diffusion peaks similar to those of the carbon structure and $CoFe_2O_4$ (PDF#46-1543) [Figure 1E][27], respectively. As can be seen from the spectra, AC exhibits typical characteristic peaks [C (002) diffraction peaks] centered at 24° with a low peak height and wide peak width, which belongs to a typical amorphous carbon structure[38]. The XRD pattern of $CoFe_2O_4$ presents characteristic peaks at 2θ = 18.46°, 30.29°, 35.55°, 43.40°, 53.76°, 57.22° and 62.79° on the spectrum of solvothermal products, which corresponded separately to the (111), (220), (311), (400), (422), (511), and (440) planes[39]. Emphatically, the synthesis conditions of solvothermal temperature and heating time exerted a nonnegligible effect on the surface energy of the $CoFe_2O_4$ crystal nucleus[15]. The spectrum of 140MAC24 was observed with the sharpened and narrow diffraction peaks of $CoFe_2O_4$, implying the highest development degree of crystalline[23]. Meanwhile, the weak and broad characteristic peaks on the 140MAC30 spectrum may be caused by the continuous variation of lattice spacing during the excessive reaction phase[15]. Additionally, the cobalt ferrite located on the MAC surface may tend to exist in the various grain sizes with the different crystallinity[15].

Table 1. Porous properties of the AC and MACs prepared under different conditions

	S_{BET}^{a} (m²/g)	S_{micro}^{b} (m²/g)	S_{meso}^{c} (m²/g)	V_{total}^{d} (cm³/g)	V_{micro}^{e} (cm³/g)	V_{meso}^{f} (cm³/g)	D_{total}^{g} (nm)	P_{meso}^{h} (%)
AC	1,503.70	470.02	1,033.68	0.951	0.240	0.711	2.448	74.76%
120MAC24	1,133.07	405.40	727.67	0.643	0.262	0.381	2.253	59.25%
140MAC18	933.51	332.94	600.57	0.619	0.191	0.428	2.616	69.14%
140MAC24	1,377.69	415.61	962.08	0.849	0.230	0.619	2.393	72.91%
140MAC30	876.42	315.65	560.77	0.582	0.179	0.403	2.617	69.24%
160MAC18	1,191.21	722.60	468.61	0.637	0.327	0.310	2.151	48.66%
160MAC24	1,355.56	425.12	930.44	0.743	0.309	0.434	2.173	58.41%
160MAC30	1,114.81	382.54	732.27	0.726	0.213	0.513	2.556	70.66%

[a]Specific surface area was calculated in P/P_0 pressure ranging from 0.05 to 0.30; [b]Micropore surface area was calculated using t-plot method; [c]Mesopore surface area was calculated using t-plot method; [d]Total pore volume at P/P_0 = 0.95; [e]Micropore volume was calculated using t-plot method; [f]V_{meso} = V_{total} - V_{micro}; [g]Average pore diameter of total pore; [h]Proportion of mesoporous. AC: Activated carbon; MACs: modified activated carbons.

Figure 2A showed the FTIR spectra of AC and MACs in a wavelength range from 4,000 to 400 cm^{-1}. The broad band at 3,430 cm^{-1} corresponded to the stretching oscillation of the -OH group, which could improve the material surface wettability[29]. The presence of C=O (1,603 cm^{-1}) and C=C (1,535 cm^{-1}) could generate the -OH group[40]. Among all samples, the peak strength of -OH on the 140MAC24 spectrum was the highest, implying the low transmission resistance of electrolytes and eminent electrochemical performance in supercapacitors[41]. Additionally, the rise of the solvothermal temperature may facilitate the depolymerization of lignocellulose, but too high temperature and heating time could cause the transformation of aliphatic groups to aromatic structure. Furthermore, the diffraction band at about 599 cm^{-1} was related to stretching vibrations of Fe-O, suggesting the successful loading of iron elements[29].

In addition, XPS spectra were performed to detect the element composition with a focus on 140MAC24. Figure 2B showed the differences of the element information using high-solution spectra. The presence of Fe 2p and Co 2p peaks distinctly suggests that $CoFe_2O_4$ was successfully synthesized on the MAC surface. The highest relative contents (4.44% and 2.57%) were measured at 140MAC24 by semi-quantitative analysis [Supplementary Table 3 and Supplementary Figure 1]. Undoubtedly, the O/C atomic ratio (0.300) also reveals that 140MAC24 had the more active sites and abundance of oxygen-containing functional groups (OFGs) than other samples[42]. This result implied the eminent surface wettability and highly efficient electron transfer, consistent with the FTIR analysis mentioned above. In depth, C-O (285.6 eV), C=O (288.5 eV) and O-H peaks (532.3 eV) were fitted by deconvolving from the spectra of C 1s and O 1s, which were conducive to increased electrolyte penetration and decreased transmission resistance [Figure 2C and D][43]. The peak at 530.6 eV corresponded to M-O-M (M=Co or Fe). The high peak strength of 140MAC24 might suggest the superior crystallin degree of $CoFe_2O_4$ NPs, which agreed well with the XRD analysis [Supplementary Table 4]. After fitting by Gaussian method, Fe (III) peaks (712.6 and 719.1 eV), Fe (II) peaks (714.4 and 726.8 eV), and its satellite peak (714.4 eV) were observed at the Fe 2p spectrum [Figure 2E and Supplementary Figure 2]. The high-resolution spectrum of Co 2p, presenting two spin-orbit doublet characteristic peaks named Co 2p$_{3/2}$ and Co 2p$_{1/2}$, was deconvoluted into peaks of Co (III) (787.9 eV), Co (II) (784.8 and 797.2 eV) and its satellite peaks (787.4 and 804.1 eV) [Figure 2F][15]. The coexistence of Co and Fe with several valent also demonstrated the successful preparation of $CoFe_2O_4$ NPs on the MAC surface.

There may be an important effect of solvothermal conditions on developing pore and $CoFe_2O_4$ NPs, and 140MAC24 was regarded as the focus and investigated emphatically. The microstructures of ACs and MACs were observed by TEM and SEM [Figure 3 and Supplementary Figure 3]. AC obtained a rougher
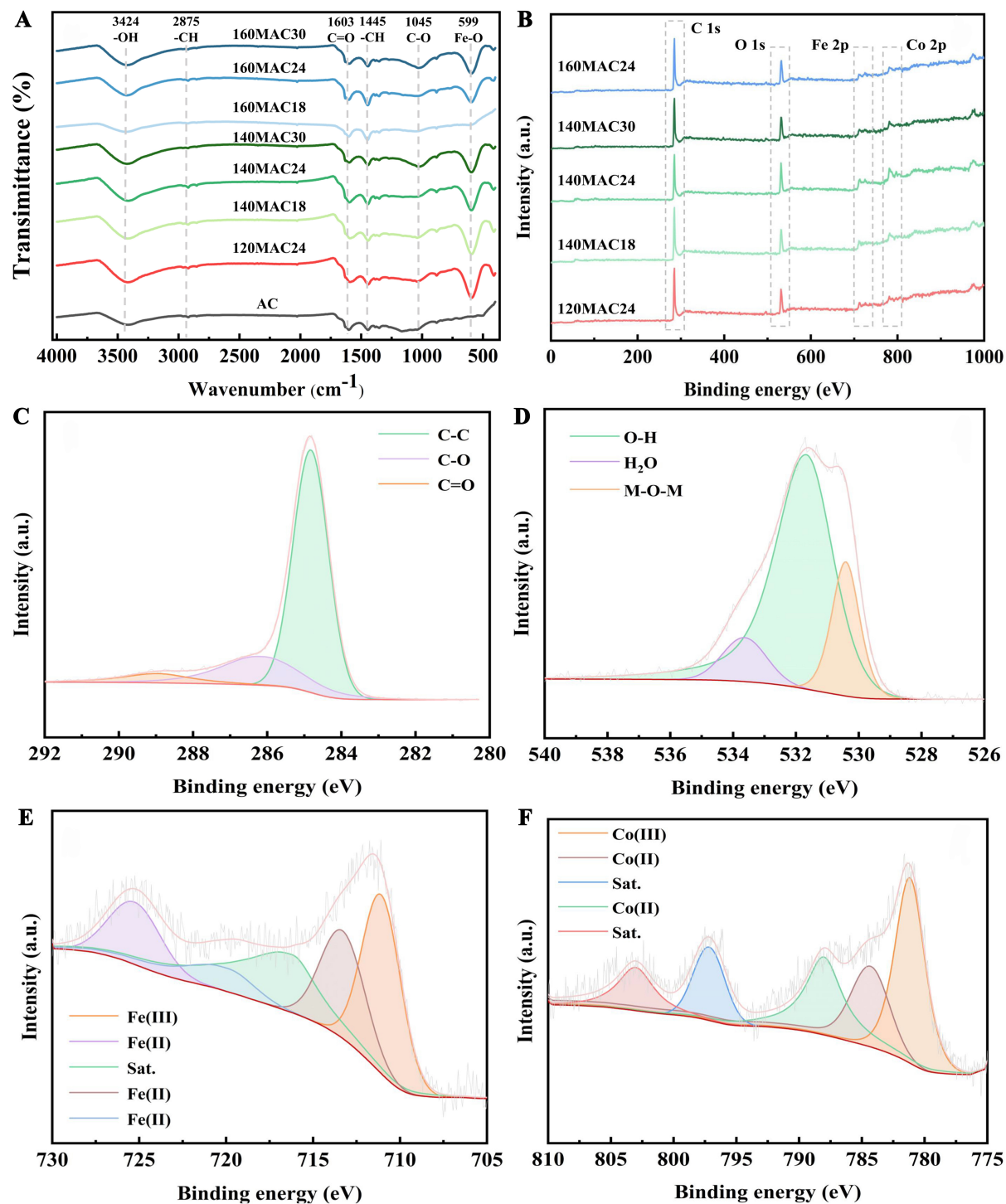
Figure 2. The FTIR spectrum and XPS spectra of AC and MACs. (A) The FTIR spectrum of AC and MACs; (B) The full-scan survey spectra of MACs; (C) The C 1s spectra of 140MAC24; (D) The O 1s spectra of 140MAC24; (E) The Fe $2p_{3/2}$ spectra of 140MAC24; (F) The Co $2p_{3/2}$ spectra of 140MAC24. FTIR: Fourier transform infrared spectroscopy; XPS: X-ray photoelectron spectroscopy; AC: activated carbon; MACs: modified activated carbons.
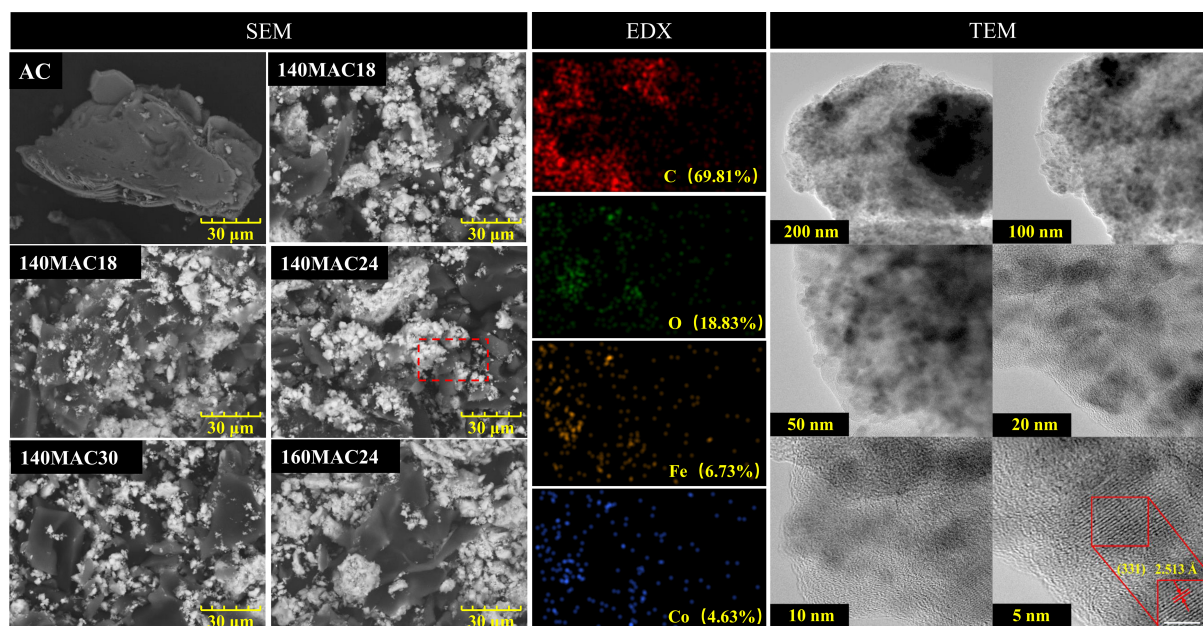
Figure 3. The SEM images of AC and MACs (×2000), EDX mapping images and TEM images of 140MAC24. SEM: Scanning electron microscopy; AC: activated carbon; MACs: modified activated carbons; EDX: energy dispersive X-ray detector; TEM: transmission electron microscope; 140MAC24: modified activated carbon heated at 140 °C for 24 h.

surface and an obviously layered carbon structure, indicating the favorable porosity[44]. Meanwhile, this structure benefited from the intense solvothermal reaction. The MAC samples exhibited the corrugated graphitic layer, resulting in the carbon structure rearrangements[45]. Meanwhile, the self-aggregation of the $CoFe_2O_4$ NPs appeared in the complexes of solvothermal reaction, which may contribute to the electrolyte transfer. According to the growth model of directionally attached crystals[15], the high-pressure condition of the solvothermal preparation technology could increase the surface energy of the crystal nucleus[41]. This theory could explain the larger size of $CoFe_2O_4$ NPs observed in the MAC sample prepared at higher solvothermal temperature. The corresponding EDX mapping of Fe and Co elements also could reveal the well-location of $CoFe_2O_4$ NPs. The TEM images could verify the SEM analysis results that the agglomeration degree of $CoFe_2O_4$ NPs evolved more intensively in the products synthesized at higher solvothermal temperature and longer heating time [Figure 3]. In addition, the pores of 140MAC24 with different extension directions indicated that ions and charges could diffuse in the carbon material through several channels[41]. Meanwhile, a distinct distribution of $CoFe_2O_4$ NPs was on the hole wall, which could provide imaginary capacitance in electrochemical applications[4]. Therefore, the capacitive performance of all samples was subsequently evaluated as the active substance of supercapacitor electrodes and tested by electrochemical measurement.

The electrochemical performance of AC and MACs

The charging and discharging behaviors of the AC and MACs were evaluated in a three-electrode configuration with Hg/HgO as the reference electrode (the potential window ranging from -1.0 to 0.2 V), 6 M KOH solution as the electrolyte, and Pt as the counter electrode. The measurement experiment of electrochemical properties was conducted using CV and GCD. Among AC and MACs, 140MAC24 exhibited a broader integral area [Figure 4A] and longer charging-discharging interval [Figure 4B] under the same scanning rate and current density conditions. This phenomenon verified that the solvothermal loading-magnetic process could promote the electrochemical properties of carbon electrodes. Figure 4A displays the charging-discharging curves of samples obtained using the CV method at a scanning rate of
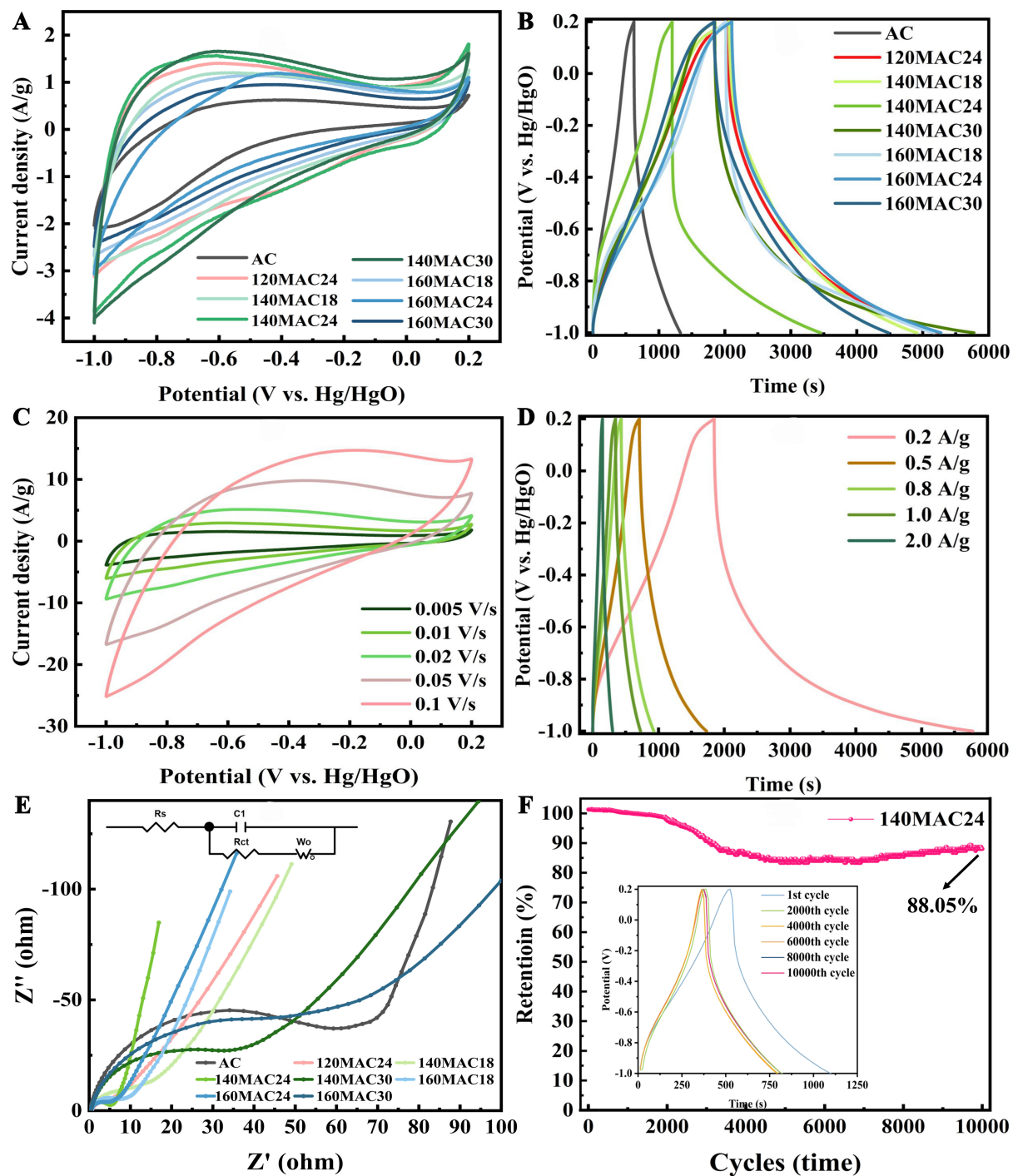
Figure 4. (A) The CV curves of AC and MACs at 0.005 V/s; (B) CV curves of 140MCA24 with different sweep rates; (C) GCD curves of AC and MACs at 0.2 A/g; (D) GCD curves of 140MAC24 with different current density; (E) EIS spectra for AC and MAC electrodes; and (F) long cycling performance of 140MAC24 electrodes. CV: Cyclic voltammetry; AC: activated carbon; MACs: modified activated carbons; 140MCA24: modified activated carbon heated at 140 °C for 24 h; GCD: galvanostatic charge-discharge; EIS: electrical impedance spectroscopy.

5 mV/s. The curve of AC presented a rectangular shape due to an electric double-layer capacitor (EDLC)[46]. In contrast, the curves of MACs revealed the obvious redox peaks due to Faradaic reaction from Fe and Co

ions, implying the generation of the pseudo capacitance[47]. Furthermore, the integral area of MACs was obviously larger than that of AC, and 140MAC24 possessed the greatest capacitance (521.88 F/g) calculated by formula (2). The result was consistent with the above XPS findings, implying the contribution of OFGs and $CoFe_2O_4$ on enhancing the electrochemical characteristic[48]. In addition, capacitance of materials escalated with the increasing solvothermal temperature and reaction time, but excessive synthesis temperature or duration could cause the collapse of the porous structure, weakening the electrochemical property [Table 2]. In Figure 4C, as the scanning rate ranged from 5 to 100 mV/s, the redox reaction peaks of CV curves gradually dampened, which was owing to the slowing ion diffusion and intercalation-deintercalation process along with the incomplete redox reaction of $CoFe_2O_4$ NPs at a rapid scan rate[34]. Meanwhile, the surrounding region on the CV curve grew with a homologous shape as the scanning rate increased. The anodic and cathodic peaks severally move towards the positive and negative potentials, suggesting the abundant active sites on the electron surface followed with fast and reversible transportation of ionic and electronic[49].

GCD could reliably evaluate the electrochemical capacitance performance of active substances. The GCD curves of materials at a current density of 0.2 A/g exhibited different inclination phenomena, indicating that the redox reactions occurred during the charging-discharging process[31]. It was noteworthy that a distinct potential drop was ascribed to internal resistance (IR) in the initial stage of the GCD curves, directly reflecting the electrical conductivity of materials [Table 2][50]. Among all products, 140MAC24 possessed the minimum IR potential drop (0.049 V), attributed to its favorable mesoporous ratio (72.91%) and monolithic conductivity agreed with the above-mentioned Roman spectroscopy and XPS analysis. With the current density ranging from 0.2 to 1 A/g, the time span between charging and discharging gradually reduced, and the corresponding capacitance of 140MAC24 ranged from 571.36 to 229.36 F/g. Furthermore, there was a noteworthy tendency of the IR potential drop as the current density amplified [Figure 4D], attributed to fewer electrolyte ion diffusion resistance in mesopores under the high current density conditions[49].

To reveal the potential mechanism of ion transfer, charge diffusion and capacitance generation, the EIS measurements were tested at open circuit potential in the frequency range of 10^5-10^{-2} Hz[51]. As illustrated in Figure 4E, there were the typical impedance curves with a quasi-semicircle at the high frequency region and a sloped line at the low frequency region[52]. Furthermore, the X-axis intercept of the plots in high frequencies (>10 Hz) often reflected the intrinsic ohmic resistance (*Rs*), and the diameter of the semicircle indicated the charge transfer resistance (*Rct*) while the angle of straight-line slope (value below 0°) at low frequencies implied the ions or electrolyte diffusion resistance [Table 2][53]. In general, mesopore structure could supply the expedited ion transfer channel and eminent charge diffusion kinetic for the surface OFGs and the redox reaction of loaded $CoFe_2O_4$ NPs, which could culminate in less resistance of material[54]. Undoubtedly, 140MAC24-containing electrodes exhibited the best electrical conductivity, the least IR (*Rs* = 1.11 Ω and *Rct* = 1.27 Ω), and the fastest electron transfer (the angle = -71°), indicating a capacitive behavior of EDLC coupled with partial pseudo capacitance[30].

The cyclical stability of electrodes could also play a vital role in the charging-discharging process, and the repeating GCD test for 10,000 cycles was conducted at a current density of 1 A/g. It was observed that 140MAC24 could display an excellent retention of 88.05% after 10,000 cycles [Figure 4F]. In detail, the capacitance of 140MAC24 electrodes initially reduced until about the 5,000th cycle. This result may be due to the irreversible decrease of effective electrochemical active area[21]. Subsequently, a rising trend of property appeared, which could contribute to the gradual penetration of electrode solution. Therefore, 140MAC24 possesses great potential for supercapacitor electrodes with well-built stability performance.

Table 2. Specific capacitance of AC and MACs calculated using CV and GCD curves

Samples	Cp (F/g)[a]	Cp (F/g)[b]	Wo (Ω)[c]	Rct (Ω)[d]	Rs (Ω)[e]
AC	231.25	258.66	21.84	30.81	1.83
120MAC24	406.69	437.20	2.95	2.41	1.26
140MAC18	365.49	427.33	5.83	5.97	1.31
140MAC24	521.88	571.36	1.84	1.36	1.11
140MAC30	317.06	384.74	12.15	11.48	1.42
160MAC18	377.76	317.04	5.16	4.29	1.36
160MAC24	276.54	378.72	3.87	3.54	1.24
160MAC30	324.64	380.88	30.64	39.84	1.61

[a]Specific capacitance was calculated at the sweep rate of 5 mV/s; [b]Specific capacitance was calculated at the current density of 0.2 A/g; [c]Warburg impedance was fitted by EIS spectrum using Z-View software; [d]Charge transfer resistance was fitted by EIS spectrum using Z-View software; [e]Solution resistance was fitted by EIS spectrum using Z-View software. AC: Activated carbon; MACs: modified activated carbon; CV: cyclic voltammetry; GCD: galvanostatic charge-discharge; EIS: electrical impedance spectroscopy.

In the practical application of devices for storing energy, the preparation cost was still a vital factor in estimating the actual performance of electrode material. Here, the basic economic assessment of AC and 140MAC24 was carried out to investigate the feasibility. Supplementary Table 5 showed the material and electricity costs, which were then added up and divided by the unit of specific capacitance. In detail, during the charging-discharging process, compared to AC, the charging-discharging of electrodes based on 140MAC24 could obviously save expenditure, which suggested the superior economic feasibility. This result was mainly due to the greater electrochemical properties of 140MAC24 than that of AC. Overall, preparing magnetic carbon material through a solvothermal heating method exhibited the splendid economic effectiveness for energy storage and could have the potential to significantly appeal to the capital market.

The electrochemical function mechanism of $CoFe_2O_4$

As can be seen in Figure 4B, the obvious asymmetry features on the charging-discharging curves of 140MAC24 during the charging and discharging process may be caused by the irreversible reaction of $CoFe_2O_4$[27]. To investigate the electrochemical function mechanism of $CoFe_2O_4$, several three-electrode systems were employed using 140MAC24 as a working electrode, and the charge and discharge under the different potential windows for 1,000 cycles were conducted. The electrode was discharged at the current density of 0.2 A/g until the potential of -1.0 V, and subsequently charged to the desired potential, which was labeled as samples with charging process. The characteristics of electrodes were further assessed using XRD, Raman, and FTIR techniques. In particular, the $CoFe_2O_4$ diffraction peaks predominated the XRD spectrum of the 140MAC24 electrode at the initial stage of -1.0 V [Figure 5A]. Then, the diffraction peaks of Fe_3O_4, Fe_2O_3, and FeO appeared on the spectrum during the charging phases, and their intensities gradually increased with the expanded potential span until 1 V. In this case, iron compounds could function as accelerators for charging by changing into the oxide form ($M^{II}O$ or $M^{III}O$) and generating faradic capacitance. However, there were few differences between the spectra of the charging potential of 0 and 0.2 V. It indicated a slight degree of redox reaction and little amount of ion transfer[37], which corresponded to the limited integral area of CV curves ranging from 0 to 0.2 V. In contrast, only the discharging region between 0.2 and 0 V exhibited obvious transformation of CoO diffraction peaks of the XRD spectrum, indicating the promoting effect of cobalt element during discharging. This phenomenon could explain why the CV curve section of discharge process included an arc of redox peak from 0.2 to 0 V and a line from 0 to -1.0 V. Additionally, the difference between diffraction peaks at the initial discharging and final charging phases could provide the evidence to the irreversible reaction of $CoFe_2O_4$ NPs.
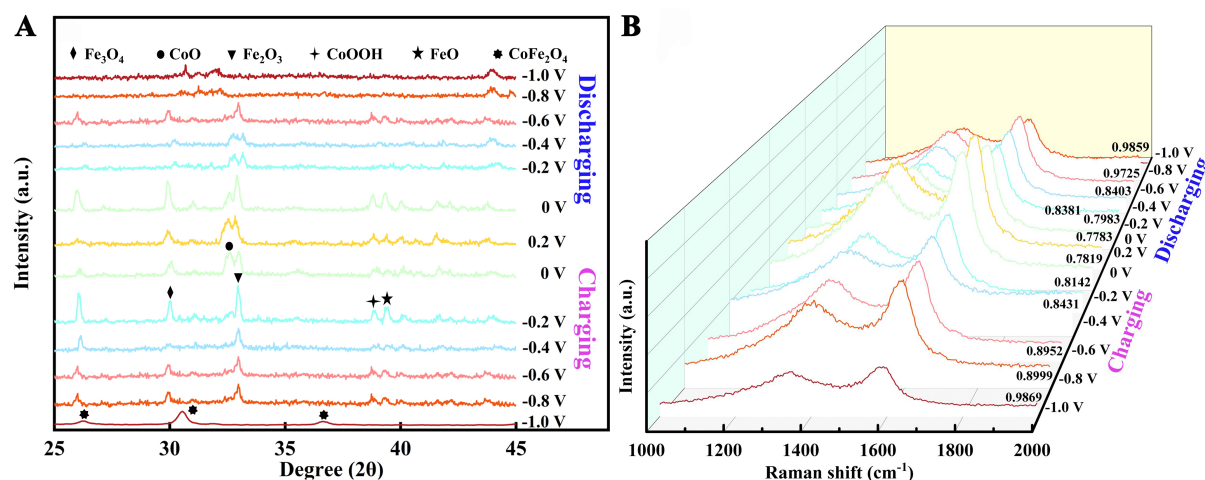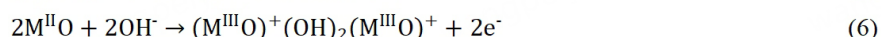
Figure 5. The (A) XRD and (B) Raman spectrums of MAC electrode after working at different voltage windows. XRD: X-ray diffractometer; MAC: modified activated carbon.

$$2M + OH^- + O_2 \rightarrow MOOH + M^{II}O + e^- \tag{5}$$

$$2M^{II}O + 2OH^- \rightarrow (M^{III}O)^+(OH)_2(M^{III}O)^+ + 2e^- \tag{6}$$

According to the XRD results, $CoFe_2O_4$ NPs could transform into the oxide and hydroxide form of metal. This phenomenon may increase the disorder degree of electrodes, which could also be assessed using Raman methods. On the spectrum of the 140MAC24 electrode at a charging potential of -1.0 V, the value of I_D/I_G (0.9869) was higher than that of 140MAC24 (0.9727) [Figure 5B]. This result may be attributed to the mix with carbon black. As the charging potential enhanced from -1.0 to 0 V, $CoFe_2O_4$ NPs reacted more strongly, which brought out the higher disorder degree. Meanwhile, the change tendencies of I_D/I_G value in the charging process from 0 to 0.2 V, discharging process from 0.2 to 0 V, and discharging process from 0.2 to -1.0 V were also coincident with the results of XRD analysis. Besides, the generation of CoOOH may be responsible for the upward tendency of -OH group abundance on FTIR spectrum of the 140MAC24 electrode [Supplementary Figure 4]. Meanwhile, the penetration of electrolyte may lead to a slight increase of -OH group between the charging potential of 0 and 0.2 V[38]. The strength of the -OH group and Fe–O bond decreased under the potential condition from 0.2 to 0 V during the discharge stage, which may be ascribed to the oxidation reaction of the oxide and hydroxide[55]. Above all, $CoFe_2O_4$ NPs on the 140MAC24 surface could generate faradic capacitance by converting to the oxide and hydroxide form of metal elements in the charging stage of -1.0 to 0 V[36], and the reaction products could conduct the redox reaction in the discharging stage of 0.2 to 0 V[49]. Therefore, $CoFe_2O_4$ NPs underwent different degrees of redox reactions in asymmetric voltage intervals during the charge-discharge stages, resulting in the irreversible charge-discharge reactions and asymmetric charge-discharge curve features. On the whole, $CoFe_2O_4$ NPs showed an excellent ability to generate pseudocapacitance during the charging phase, indicating the great feasibility of using as anode material.

The supercapacitive properties of MAC

For evaluating the application of electrode-based 140MAC24, the supercapacitors were assembled in the form of coin batteries (CB). Generally, the operating potential window is essential for the performance of energy storing devices[18]. Therefore, the CV measurement with various operating voltage windows (0-1.8 V) was conducted to obtain the proper condition, and the results were shown in Figure 6A. Specifically, a
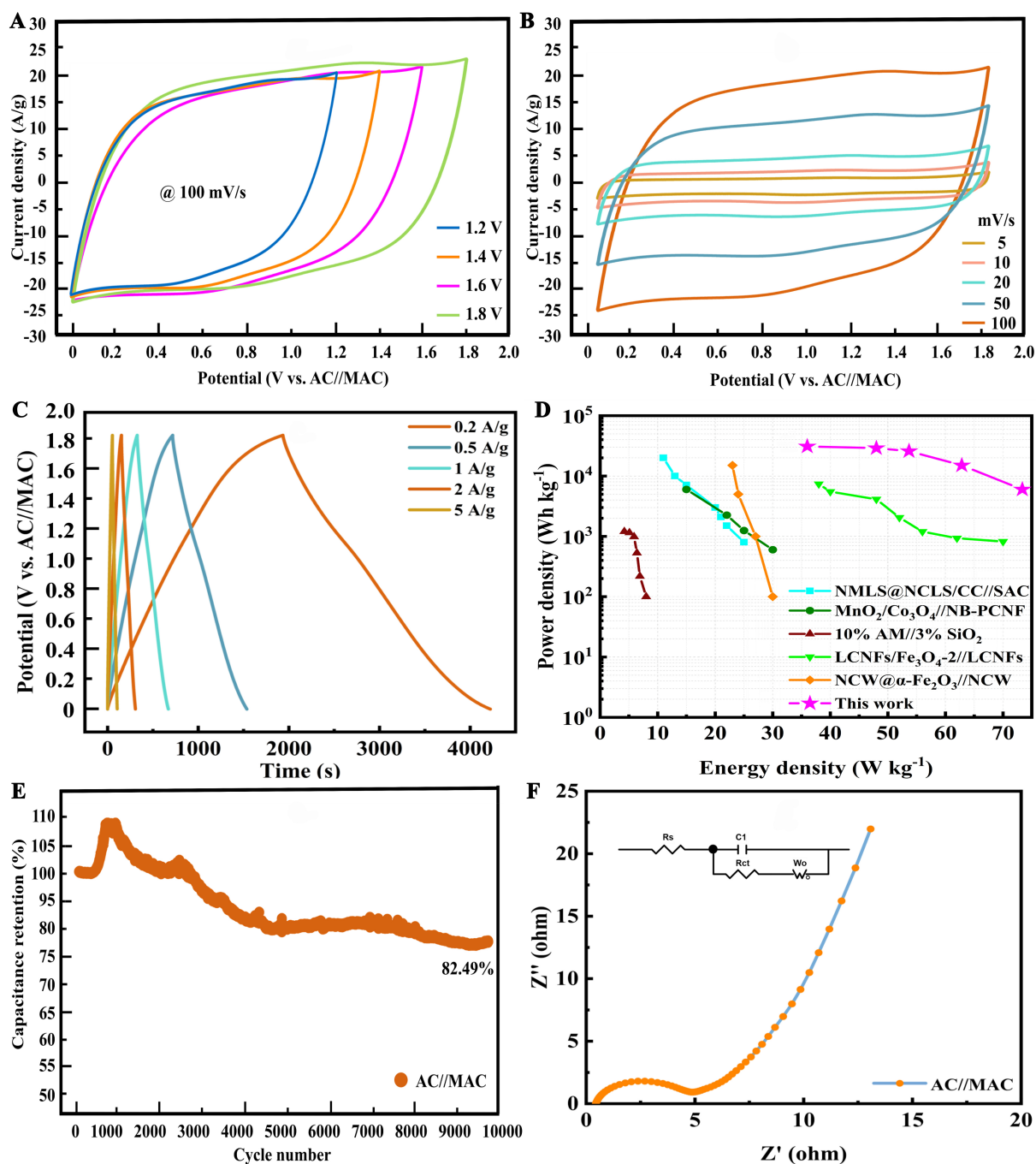
Figure 6. The supercapacitive properties of AC/MAC in the CB system. (A) The CV curves of CB measured at different voltage windows; (B) the CV curves of CB at different scan rates (5-100 mV/s); (C) the GCD curves of CB at different current densities; (D) the Ragone plot CB compared with other studies; (E) the cycling stability of CB; and (F) the electrochemical impedance spectroscopy of CB[10,12,16,35]. AC: Activated carbon; MAC: modified activated carbon; CB: coin battery; CV: cyclic voltammetry; GCD: galvanostatic charge-discharge.

favorable association was between the amount of electric charge calculated by the integral area of CV region and the potential interval up to 1.8 V. The CV plots were measured at several scanning rates of 5-100 mV/s in the optimum working voltage window of 1.8 V. The CV curves showed distinct redox peaks, and the peak location gradually moved towards low potential as the scanning rate ranged from 5 to 100 mV/s

[Figure 6B]. Meanwhile, the specific capacitance increased to the maximum of 171.31 F/g at the scanning rate of 5 mV/s, suggesting the outstanding reversibility of redox reaction and fast electron diffusion kinetic of faradic process[41].

The charging-discharging feature was analyzed at the various current densities, with the curves represented in Figure 6C. The peaks of the redox reaction were linked to the modest change in the symmetrical shape of the curves. This characteristic indicated the stable structure performance of electrodes in the charging-discharging process. Moreover, an obvious potential drop appeared on the discharging stage under the different current densities, which was up to 1.8 V at the current density of 0.2 A/g. The supercapacitive property of fabricated devices had been evaluated using formula (3), which displayed the highest value of 156.60 F/g. The specific capacitance was lower than that of a single electrode, and the potential drop in a button battery was around double that of a three-electrode system. This effect could result from the resistance of the separator and electrode, which limited the ion and charge transfer[19]. Then, the energy density was estimated and compared with the studies about energy storing devices [Figure 6D]. The higher values of energy densities calculated at the current density of 0.2 A/g were up to 73.36 Wh/kg, higher than those supercapacitors assembled with pure or modified carbon[45,55-60]. Meanwhile, the assembled supercapacitor conducted the CGD test for 10,000 cycles, and the capacitance could maintain a retention rate of 82.49% with a gradual decrease trend [Figure 6E].

The EIS spectra of a coin system were conducted to investigate the physical properties such as transfer kinetics of electrolytes and intrinsic resistance of supercapacitors. The results were represented in the form of a Nyquist plot [Figure 6F], which resembled the equivalent circuit in the three-electrode configuration. In detail, the charge transfer resistance of assembled devices (1.5 Ω) was similar to that in the single electrode system, which demonstrated the outstanding kinetic of ion transfer[34].

CONCLUSION

The present research investigated the role of solvothermal temperature and holding heating time in the synthetization of $CoFe_2O_4$ on the characteristic and electrochemical performance of carbon composites. Prepared under the condition of 140 °C reaction temperature and holding for 24 h, 140MAC24 displayed a greater ratio of mesopore distributions (72.91%), better-developed pore structure (SSA of 1,377.69 m^2/g), outstanding graphitization degree (I_D/I_G of 0.9727), and anchored content of $CoFe_2O_4$, which implies the well-built properties as a supercapacitor electrode. The experiment results of three electrode configurations demonstrated the high specific capacitance of the 140MAC24 electrode (571.36 F/g at the current density of 0.2 A/g). Besides, it displayed the splendid feasibility of economic assessment. Meanwhile, $CoFe_2O_4$ NPs could convert to the feature of metal oxide and hydroxide of iron and cobalt elements to create faradic capacitance during charging and discharging, respectively. The assembled battery-type asymmetric supercapacitor using 140MAC24 as an anode and AC as a cathode could display an outstanding energy density of 43.5 KW/kg and a rate of 82.45% after 10,000 cycles. This study could provide some technique support for producing carbon materials for supercapacitor applications and expanding the scope of energy storage within the realm of supercapacitor applications.

DECLARATIONS

Authors' contributions

Conceived the idea of the project: Zhu MQ
Made substantial contributions to the conception and design of the study, performed data analysis and interpretation, and wrote the draft of manuscript: Qu Q
Performed data acquisition and provided administrative, technical, and material support: Chen Z, Sun GT
Discussed and revised the manuscript: Qiu L
Finalized the manuscript: Zhu MQ

Availability of data and materials

The data supporting this article have been included as part of the Supplementary Materials.

Financial support and sponsorship

Conflicts of interest

All authors declared that there are no conflicts of interest.

Ethical approval and consent to participate

Not applicable.

Consent for publication

Not applicable.

Copyright

REFERENCES

1. Pohlmann S. Metrics and methods for moving from research to innovation in energy storage. *Nat Commun* 2022;13:1538. DOI PubMed PMC
2. Ding Y, Li Y, Dai Y, et al. A novel approach for preparing in-situ nitrogen doped carbon via pyrolysis of bean pulp for supercapacitors. *Energy* 2021;216:119227. DOI
3. Gogoi D, Makkar P, Das MR, Ghosh NN. $CoFe_2O_4$ nanoparticle decorated hierarchical biomass derived porous carbon based nanocomposites for high-performance all-solid-state flexible asymmetric supercapacitor devices. *ACS Appl Electron Mater* 2022;4:795-806. DOI
4. Bhosale R, Bhosale S, Chavan V, Jambhale C, Kim D, Kolekar S. hybrid supercapacitors based on nanoporous carbon and $CoFe_2O_4$ derived from a bimetallic organic framework. *ACS Appl Nano Mater* 2024;7:2244-57. DOI
5. Hu B, Xu J, Fan Z, et al. Covalent organic framework based lithium-sulfur batteries: materials, interfaces, and solid-state electrolytes. *Adv Energy Mater* 2023;13:2203540. DOI
6. Wang J, Xi L, Peng C, et al. Recent progress in hard carbon anodes for sodium-ion batteries. *Adv Eng Mater* 2024;26:2302063. DOI
7. Chen J, Adit G, Li L, Zhang Y, Chua DHC, Lee PS. Optimization strategies toward functional sodium-ion batteries. *Energy Environ Mater* 2023;6:e12633. DOI
8. Wu X, Zhao Y, Li H, Zhou C, Wang X, Du L. Sulfurized polyacrylonitrile as cathodes for advanced lithium-sulfur batteries: advances in modification strategies. *Nanoscale* 2024;16:5060-78. DOI
9. Han J, Varzi A, Passerini S. The emergence of aqueous ammonium-ion batteries. *Angew Chem Int Ed* 2022;61:e202115046. DOI PubMed PMC
10. Geng X, Hou X, He X, Fan HJ. Challenges and strategies on interphasial regulation for aqueous rechargeable batteries. *Adv Energy Mater* 2024;14:2304094. DOI
11. Kao C, Liu J, Ye C, Zhang S, Hao J, Qiao S. Building fast and selective Zn ion channels for highly stable quasi-solid-state Zn-ion

batteries. *J Mater Chem A* 2023;11:23881-7. DOI

12. Yi M, Jing M, Yang Y, et al. Recent developments of carbon dots for advanced zinc-based batteries: a review. *Adv Funct Mater* 2024. DOI

13. Du B, Shi X, Zhu H, et al. Preparation and characterization of bifunctional wolfsbane-like magnetic Fe_3O_4 nanoparticles-decorated lignin-based carbon nanofibers composites for electromagnetic wave absorption and electrochemical energy storage. *Int J Biol Macromol* 2023;246:125574. DOI PubMed

14. Jain A, Michalska M, Zaszczyńska A, Denis P. Surface modification of activated carbon with silver nanoparticles for electrochemical double layer capacitors. *J Energy Storage* 2022;54:105367. DOI

15. Liao Z, Su HY, Cheng J, Sun GT, Zhu L, Zhu MQ. $CoFe_2O_4$- mesoporous carbons derived from *Eucommia ulmoides* wood for supercapacitors: comparison of two activation method and composite carbons material synthesis method. *Ind Crop Prod* 2021;171:113861. DOI

16. Sun L, Gong Y, Li D, Pan C. Biomass-derived porous carbon materials: synthesis, designing, and applications for supercapacitors. *Green Chem* 2022;24:3864-94. DOI

17. Qin H, Liu P, Chen C, Cong HP, Yu SH. A multi-responsive healable supercapacitor. *Nat Commun* 2021;12:4297. DOI PubMed PMC

18. Kumar S, Saeed G, Zhu L, Hui KN, Kim NH, Lee JH. 0D to 3D carbon-based networks combined with pseudocapacitive electrode material for high energy density supercapacitor: a review. *Chem Eng J* 2021;403:126352. DOI

19. Kumari R, Kumar Sharma S, Singh V, Ravi Kant C. Facile, two-step synthesis of activated carbon soot from used soybean oil and waste engine oil for supercapacitor electrodes. *Mater Today Proceed* 2022;67:483-9. DOI

20. Luo N, Wang J, Zhang D, et al. Inorganic nanoparticle-enhanced double-network hydrogel electrolytes for supercapacitor with superior low-temperature adaptability. *Chem Eng J* 2024;479:147741. DOI

21. He Q, He R, Zia A, et al. Self-promoting energy storage in balsa wood-converted porous carbon coupled with carbon nanotubes. *Small* 2022;18:2200272. DOI

22. Shah SS, Aziz MA, Rasool PI, et al. Electrochemical synergy and future prospects: advancements and challenges in MXene and MOFs composites for hybrid supercapacitors. *Sustain Mater Technol* 2024;39:e00814. DOI

23. Rohith R, Prasannakumar AT, Manju V, Mohan RR, Varma SJ. Flexible, symmetric supercapacitor using self-stabilized dispersion-polymerised polyaniline/V_2O_5 hybrid electrodes. *Chem Eng J* 2023;467:143499. DOI

24. Duan G, Zhang H, Zhang C, Jiang S, Hou H. High mass-loading α-Fe_2O_3 nanoparticles anchored on nitrogen-doped wood carbon for high-energy-density supercapacitor. *Chin Chem Lett* 2023;34:108283. DOI

25. Zhang X, Yan G, Li Z, et al. Self-supported heterojunction nanofibrous membranes for high-performance flexible asymmetric capacitors. *Appl Surf Sci* 2024;648:159059. DOI

26. Sharifi S, Rahimi K, Yazdani A. Largely enhanced pseudocapacitance by a facile in-situ decoration of MoS_2 nanosheets with $CoFe_2O_4$ nanoparticles. *J Energy Storage* 2023;72:108499. DOI

27. Xia C, Ren T, Darabi R, et al. Spotlighting the boosted energy storage capacity of $CoFe_2O_4$/GRaphene nanoribbons: a promising positive electrode material for high-energy-density asymmetric supercapacitor. *Energy* 2023;270:126914. DOI

28. He C, Huang M, Zhao L, et al. Enhanced electrochemical performance of porous carbon from wheat straw as remolded by hydrothermal processing. *Sci Total Environ* 2022;842:156905. DOI

29. Qu Q, Qiu L, Li M, Sun G, Chen H, Guo X. Synergistic effects of pyrolysis temperature, iron ion concentration and solid/liquid ratio on the properties and Cr(VI) removal performance of magnetic carbon. *J Water Process Eng* 2023;53:103785. DOI

30. Bian Z, Wang H, Zhao X, et al. Optimized mesopores enable enhanced capacitance of electrochemical capacitors using ultrahigh surface area carbon derived from waste feathers. *J Colloid Interface Sci* 2023;630:115-26. DOI

31. Aydın H, Kurtan Ü, Üstün B, Koç SN. One-pot synthesis of cobalt pyrophosphate nanoparticles combined with mesoporous carbon for asymmetric supercapacitors. *Mater Chem Phys* 2022;290:126392. DOI

32. Chen X, Sawut N, Chen K, et al. Filling carbon: a microstructure-engineered hard carbon for efficient alkali metal ion storage. *Energy Environ Sci* 2023;16:4041-53. DOI

33. Zhu L, Wang Q, Wang H, Zhao F, Li D. One-step chemical activation facilitates synthesis of activated carbons from Acer truncatum seed shells for premium capacitor electrodes. *Ind Crop Prod* 2022;187:115458. DOI

34. Guo T, Zhou D, Pang L, Sun S, Zhou T, Su J. Perspectives on working voltage of aqueous supercapacitors. *Small* 2022;18:e2106360. DOI PubMed

35. Krishnamoorthy K, Pazhamalai P, Mariappan VK, Nardekar SS, Sahoo S, Kim SJ. Probing the energy conversion process in piezoelectric-driven electrochemical self-charging supercapacitor power cell using piezoelectrochemical spectroscopy. *Nat Commun* 2020;11:2351. DOI PubMed PMC

36. Liang Z, Hong Z, Xie M, Gu D. Recent progress of mesoporous carbons applied in electrochemical catalysis. *New Carbon Mater* 2022;37:152-79. DOI

37. Cui J, Zhang Y, Cao Z, et al. Nanoporous carbon nanowires derived from one-dimensional metal-organic framework core-shell hybrids for enhanced electrochemical energy storage. *Appl Surf Sci* 2022;576:151800. DOI

38. Piwek J, Slesinski A, Fic K, et al. High frequency response of adenine-derived carbon in aqueous electrochemical capacitor. *Electrochim Acta* 2022;424:140649. DOI

39. Das A, Girija Shankar E, Ramulu B, Su Yu J. Electrochemical performance of asymmetric supercapacitor with binder-free $Co_xMn_{3-x}Se$

4 and radish-derived carbon electrodes using $K_3[Fe(CN)_6]$ additive in electrolyte. *Chem Eng J* 2022;448:137725. DOI

40.   Kolanowski Ł, Graś-ligocka M, Krawczyk P, Buchwald T, Lota K, Lota G. Ozonation with ammoxidation as a method of obtaining O, N-doped carbon electrode material to electrochemical capacitors. *Electrochim Acta* 2022;413:140130. DOI

41.   Gan G, Fan S, Li X, et al. Effects of oxygen functional groups on electrochemical performance of carbon materials for dechlorination of 1,2-dichloroethane to ethylene. *Chem Eng J* 2022;434:134547. DOI

42.   Benoy SM, Pandey M, Bhattacharjya D, Saikia BK. Recent trends in supercapacitor-battery hybrid energy storage devices based on carbon materials. *J Energy Storage* 2022;52:104938. DOI

43.   Mazzucato M, Isse AA, Durante C. Dissociative electron transfer mechanism and application in the electrocatalytic activation of organic halides. *Curr Opin Electrochem* 2023;39:101254. DOI

44.   Madhu R, Periasamy AP, Schlee P, Hérou S, Titirici M. Lignin: A sustainable precursor for nanostructured carbon materials for supercapacitors. *Carbon* 2023;207:172-97. DOI

45.   Xu M, Zhu X, Lai Y, et al. Production of hierarchical porous bio‑carbon based on deep eutectic solvent fractionated lignin nanoparticles for high-performance supercapacitor. *Appl Energy* 2024;353:122095. DOI

46.   Ortiz-olivares RD, Lobato-peralta DR, Arias D, et al. Production of nanoarchitectonics corncob activated carbon as electrode material for enhanced supercapacitor performance. *J Energy Storage* 2022;55:105447. DOI

47.   Rimal V, Kumar Srivastava P. Review on electrochemical kinetics of carbon dots. *Mater Today Proceed* 2022;68:2691-4. DOI

48.   Xing F, Bi Z, Su F, Liu F, Wu Z. Unraveling the design principles of battery-supercapacitor hybrid devices: from fundamental mechanisms to microstructure engineering and challenging perspectives. *Adv Energy Mater* 2022;12:2200594. DOI

49.   Wang M, Yang J, Liu S, et al. Nitrogen-doped porous carbon electrode for aqueous iodide redox supercapacitor. *Chem Eng J* 2023;451:138501. DOI

50.   Sekhar SC, Ramulu B, Arbaz SJ, Hussain SK, Yu JS. One-pot hydrothermal-derived NiS_2-$CoMo_2S_4$ with vertically aligned nanorods as a binder-free electrode for coin-cell-type hybrid supercapacitor. *Small Methods* 2021;5:e2100335. DOI

51.   Zardkhoshoui A, Ameri B, Saeed Hosseiny Davarani S. Fabrication of hollow $MnFe_2O_4$ nanocubes assembled by CoS_2 nanosheets for hybrid supercapacitors. *Chem Eng J* 2022;435:135170. DOI

52.   Huang Z, Jiang J, Li W, et al. Stabilizing sulfur doped manganese oxide active sites with phosphorus doped hierarchical nested square carbon for efficient asymmetric supercapacitor. *Chem Eng J* 2023;468:143574. DOI

53.   Chen R, Tang H, He P, et al. Interface engineering of biomass-derived carbon used as ultrahigh-energy-density and practical mass-loading supercapacitor electrodes. *Adv Funct Mater* 2023;33:2212078. DOI

54.   Wei Y, Zhou J, Yang L, Gu J, Chen Z, He X. N/S co-doped interconnected porous carbon nanosheets as high-performance supercapacitor electrode materials. *New Carbon Mater* 2022;37:707-15. DOI

55.   Li P, Feng C, Li H, Zhang X, Zheng X. Facile fabrication of carbon materials with hierarchical porous structure for high-performance supercapacitors. *J Alloy Compd* 2021;851:156922. DOI

56.   Chang C, Li M, Niu P, Zhang L, Wang S. A facile dual-functional hydrothermal-assisted synthesis strategy of hierarchical porous carbon for enhanced supercapacitor performance. *Sustain Mater Technol* 2021;28:e00265. DOI

57.   Farma R, Tania Y, Apriyani I. Conversion of hazelnut seed shell biomass into porous activated carbon with KOH and CO_2 activation for supercapacitors. *Mater Today Proceed* 2023;87:51-6. DOI

58.   He W, Li J, Zhang Y, Yang J, Zeng T, Yang N. High-performance supercapacitors using hierarchical and sulfur-doped trimetallic NiCo/NiMn layered double hydroxides. *Small Methods* 2023:e2301167. DOI

59.   Ahmad T, Murtaza, Shah SS, et al. Preparation and electrochemical performance of convolvulus arvensis-derived activated carbon for symmetric supercapacitors. *Mater Sci Eng B* 2023;292:116430. DOI

60.   Zhang W, Li W, Li S. Self-template activated carbons for aqueous supercapacitors. *Sustain Mater Technol* 2023;36:e00582. DOI